Energy 328 (2025) 136417

Contents lists available at ScienceDirect

Energy

journal homepage: www.elsevier.com/locate/energy

Optimization of dynamic compressed CO_2 energy storage system: The role of supercritical fluid properties

Yuandong Guo [a,b], Jinliang Xu [a,b,c], Xiongjiang Yu [a,b,c,*], Enhui Sun [a,c], Jian Xie [a,b,c], Guanglin Liu [a,c]

[a] Beijing Key Laboratory of Multiphase Flow and Heat Transfer for Low Grade Energy Utilization, North China Electric Power University, Beijing, 100026, China
[b] Beijing Huairou Laboratory, Beijing, 101400, China
[c] Key Laboratory of Power Station Energy Transfer Conversion and System (North China Electric Power University), Ministry of Education, Beijing, 102206, China

ARTICLE INFO

Handling editor: Ruzhu Wang

Keywords:
Compressed CO_2 energy storage
Supercritical CO_2 tank
Discharging optimization method
Pseudo-critical temperature

ABSTRACT

The rising demand for efficient energy storage has spurred the development of technologies like liquefied CO_2 energy storage systems, which reduce pressure fluctuations by storing CO_2 as a liquid. Traditionally, the storage temperature of CO_2 is the saturation liquid temperature because evaporation compensation helps maintain stable pressure during gas release. However, the liquefied CO_2 energy storage system suffers low round-trip efficiency due to low temperature for liquefaction. Here, we propose a compressed CO_2 energy storage (CCES) system using the properties of supercritical fluids to extend the discharging time. The core optimization strategy involves storing sCO_2 near the pseudo-critical temperature during the charging process, which facilitates more efficient expansion of sCO_2 during the discharging process, thereby extending the discharging time. Then, a dynamic CCES system incorporating three-stage compression and three-stage expansion are proposed. With the compression power consumption of 100 MW, the high-pressure tank is set to be 14.00 MPa and 7.50 MPa before and after discharging. Based on the discharging optimization method, the round-trip efficiency improves from 66.50 % to 69.32 %, and the discharging time extends from 0.96 h to 3 h. Our work fills the gap in the selection criteria for storage parameters of CCES system, and significantly improving the performance of CCES system.

1. Introduction

Electricity is a crucial driver of global economic development, with the majority of electrical energy being derived from fossil fuels [1]. Over the past two centuries, the rapid consumption of traditional fossil energy has led to global issues such as climate warming, environmental pollution, and energy crises [2]. These problems have severely impacted the sustainable development of the global economy. Against this backdrop, the development of renewable energy sources such as solar and wind power has become a growing trend. However, the intermittency and variability of renewable energy sources pose challenges to the operation of power grids [3]. Therefore, the development of energy storage technologies is an effective solution to address these issues [4,5].

The main large-scale energy storage technologies are pumped storage and compressed air energy storage (CAES) [6]. Currently, pumped storage is a highly mature commercial technology, with an installed capacity of 39.8 GW in China, accounting for 86 % of the total energy storage capacity [7]. However, the future development potential of pumped storage is limited by geographical conditions, environmental impacts, and other challenges [8]. In contrast, compressed air energy storage (CAES) has advantages in terms of site selection requirements and cost [9]. Traditional CAES systems are supplemented by fossil fuels, which provide the necessary heat, resulting in low efficiency and continued environmental pollution [10,11]. To address these issues, adiabatic CAES (A-CAES) systems have been proposed, where heat generated during compressor compression is stored during the charging process and used to heat the high-pressure air during the discharging process [12]. Due to the low air density in high-pressure tanks, the system faces challenges such as low energy storage density and high investment costs [13]. Guizzi et al. [14] proposed a liquid air energy storage (LAES) system to improve storage density. Despite this, the physical properties of air, including its relatively low liquefaction and supercritical temperatures, create challenges in both storing the working fluid and liquefying the cooling source [15].

* Corresponding author. Beijing Key Laboratory of Multiphase Flow and Heat Transfer for Low Grade Energy Utilization, North China Electric Power University, Beijing, 100026, China.
E-mail address: yuxiongjiang@ncepu.edu.cn (X. Yu).

https://doi.org/10.1016/j.energy.2025.136417
Received 13 March 2025; Received in revised form 23 April 2025; Accepted 3 May 2025
Available online 8 May 2025
0360-5442/

Carbon dioxide (CO_2), has become an outstanding candidate for the working fluid in compressed gas energy storage systems due to its excellent physical properties [16]. Specifically, CO_2 can reach its critical condition (31.3 °C, 7.38 MPa) or undergo liquefaction much easier compared to air whose critical point being −141 °C, 3.77 MPa. Additionally, supercritical CO_2 (sCO_2) possesses favorable physical properties, such as low viscosity, high density, high thermal stability, non-toxicity, and non-flammability, making it an safe and environmentally friendly option for engineering applications [17]. Therefore, compressed carbon dioxide energy storage (CCES) system becomes a viable alternative to CAES [18,19].

Similar to CAES, CCES system relies on the CO_2 compression exothermic process for energy storage and the expansion endothermic process for energy release [20]. The working principle involves compressing CO_2 to convert electrical energy into pressure potential and thermal energy. Energy is stored through high-pressure CO_2, compressed heat, and expansion cold energy [21]. During energy release, the compressed heat is used to heat the high-pressure CO_2, which then undergoes expansion in a turbine to perform work and release energy. The key difference is that the CAES system is an open-cycle energy storage system, where air is directly drawn from the environment and expelled through the turbine expansion [22]. In contrast, CO_2 cannot be obtained in large quantities from the environment, so the CCES system operates as a closed-cycle system, requiring an additional container to store the low-pressure CO_2.

The key issue encountered in the development of CCES system is how to mitigate pressure variations in the storage tank during the discharging process. As CO_2 is discharged from the storage tank, the continuous decrease in pressure and temperature causes components like the compressor and turbine to operate under off-design conditions, thereby reducing their efficiency [23]. If the pressure fluctuations of CO_2 within the storage tank are mitigated, the energy discharge duration can be extended, and the round-trip efficiency can be improved. In this context, He et al. [24] proposed using an aquifer to maintain constant pressure in the CCES system, with low-pressure and high-pressure chambers stored at depths of 100 m and 1700 m, respectively. After optimizing the compression and expansion ratios for multi-stage compression and expansion processes, an efficiency of 74.00 % can be achieved. Similarly, some researchers have proposed a constant-pressure CCES system with gas storage chambers placed underwater [25]. However, such constant-pressure storage solutions depend on favorable geological conditions, limiting their applicability. Further experimental validation is required to address potential challenges and risks.

For the low-pressure side of CCES system, a mature solution involves storing low-pressure CO_2 in a large flexible gas holder, where the temperature and pressure of the working fluid are nearly the same as the surrounding environment [26,27]. Therefore, the CO_2 in the gas holder can be considered to be released at a constant pressure and temperature. Since the investment cost of the gas holder is much lower than that of high-pressure storage tanks, researchers have not considered the volume of the gas holder when calculating the energy storage density (*ESD*) [27].

To increase *ESD*, some researchers have proposed a liquefied CO_2 energy storage (LCES) system [28–30], in which CO_2 is stored as a liquid whose temperature is set to the saturated liquid temperature, allowing part of the liquid to rapidly expand into gas during the discharge process to reduce pressure fluctuations within the tank. Although the LCES system incorporates the processes of CO_2 liquefaction and gasification, it creates a significant mismatch between the CO_2 and the cooling working fluid. Consequently, the round-trip efficiency of the system typically falls below 60 % [18,19]. When CO_2 reaches a supercritical state, phase changes can be avoided, and the heat exchange temperature range is better matched, resulting in higher efficiency. However, there has been limited research focusing on the storage conditions for CO_2 [31–33].

While prior studies have drawn parallels between subcritical CO_2 in saturated liquid states and supercritical CO_2 (sCO_2) in liquid-like regimes to hypothesize enhanced expansion capacity [32,33], critical knowledge gaps persist in characterizing the thermodynamic behavior of sCO_2 during dynamic discharging processes. Existing analyses frequently oversimplify sCO_2 as an ideal gas [32,33], neglecting the non-linear variations in pressure and temperature inherent in supercritical fluids. This simplification fundamentally misrepresents the thermophysical properties of sCO_2 near the pseudo-critical region, where drastic density gradients ($\partial\rho/\partial T$) and specific heat capacity (Cp) dominate energy transfer mechanisms [34]. Furthermore, the assumption of quasi-static discharge conditions fails to account for the transient coupling between liquid-like and gas-like states, as well as the dynamic pressure decay within the storage tank—a phenomenon critical to optimizing *ESD* and round-trip efficiency. Dong et al. [35], based on molecular dynamics simulations of supercritical argon molecules, found that when the working fluid is in a supercritical state, the difference between gas and liquid densities is small. Compared to the subcritical state, liquid-like molecules must overcome greater potential energy to transition into gas-like molecules. Moreover, the threshold for the minimum nucleation energy required for pseudo-boiling increases with pressure, whereas in the subcritical range, it remains roughly constant. The microscopic behavior of supercritical fluids indicates that more energy is required for molecules to break free from their interactions in the supercritical state [35]. This indicates that the criteria applicable under subcritical conditions may not necessarily apply under supercritical conditions, such as the selection of storage temperature for CO_2 in HPT. Therefore, we conducted a thermodynamic study incorporating the actual physical properties of sCO_2 to enhance the *ESD* of CCES system.

Here, a dynamic CCES system with three-stage compression and three-stage expansion is developed. On the low-pressure side, CO_2 is stored in a gas holder to maintain constant pressure. On the high-pressure side, CO_2 is stored as a supercritical fluid in the high-pressure tank (HPT), with the system operating under pressure-slide conditions. The main contributions of this study are as follows: (1) The innovative storage parameter criteria is proposed. Through thermodynamic analysis, we propose criteria for selecting parameter for sCO_2. This approach lays the foundation for optimizing the performance and energy storage density of the CCES system. (2) The dynamic CCES system is developed. Based on thermodynamic principles, we have successfully established a dynamic CCES system. (3) The system performance is analyzed and optimized. When the sCO_2 storage temperature increases from 35 °C to 75 °C under different pressures, the *ESD* first increases, reaches a maximum, and then decreases. This parabolic turning point occurs near the pseudo-critical point due to significant changes in fluid properties.

The study is divided into five sections. The proposed CCES system and discharging optimization method are described in section 2. Section 3 introduces the thermodynamic models of key components. Section 4 discusses the results of the simulations. The main conclusions are summarized in section 5.

2. Theoretical foundation and system description

2.1. Description of discharging principle

For a compressed energy storage system, more CO_2 released during the discharging process leads to more out-put work when the storage pressure ($P_{s,dis}$), discharge end pressure ($P_{e,dis}$), and tank volume (V) are fixed. Fig. 1a and b shows the schematic diagram and *T-s* diagram of the discharging process for a tank containing subcritical CO_2, respectively. Given the initial parameters inside the tank at the start of discharge, such as storage pressure $P_{s,dis}$, storage vapor quality $x_{s,dis}$, storage CO_2 density $\rho_{s,dis}$. Then, assuming an isentropic process, the parameters at the end of discharge (such as discharge end vapor quality $x_{e,dis}$ and discharge end density $\rho_{e,dis}$) can be determined based on the final pressure $P_{e,dis}$. Fig. 1c shows the variation in CO_2 density with vapor quality at different pressures. As the vapor quality increases from 0 to 1,

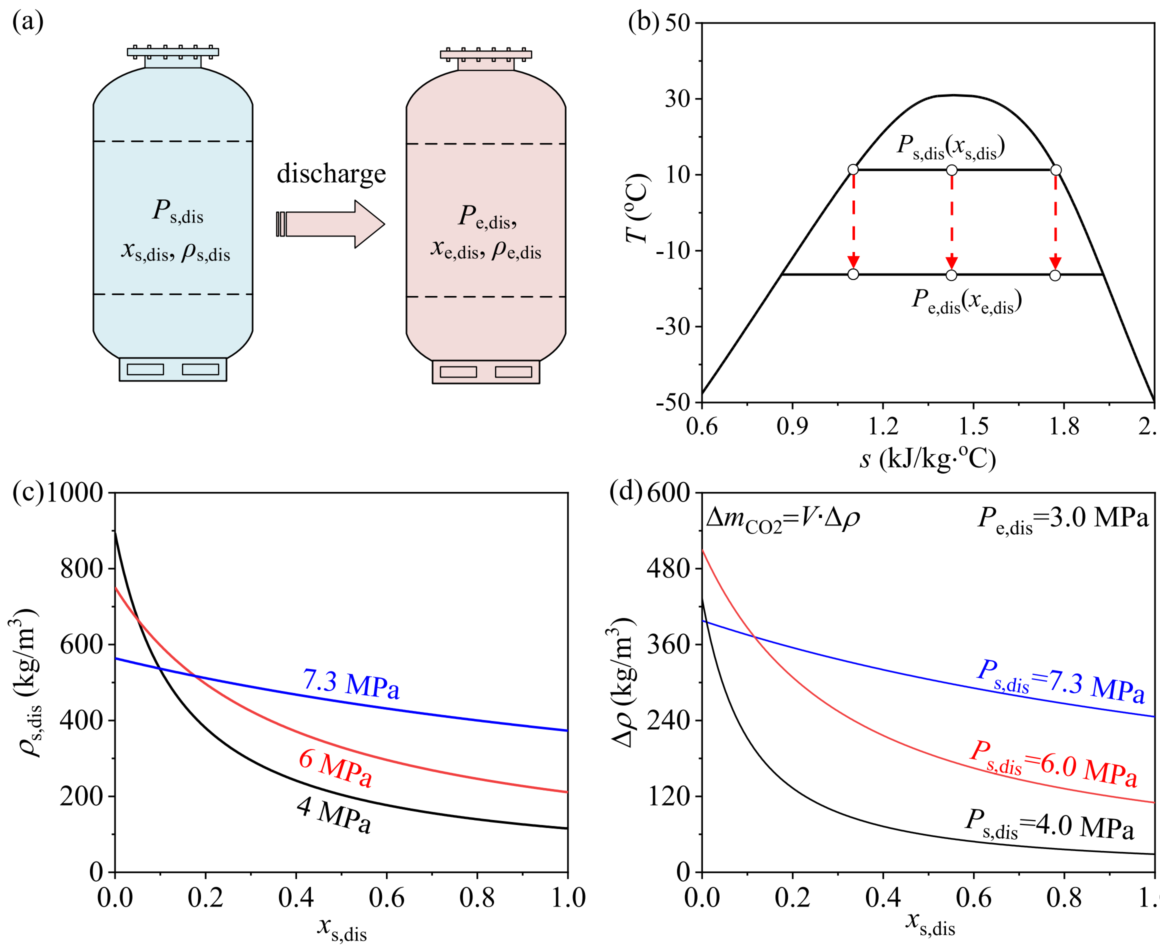

Fig. 1. Principles for selecting storage temperature of subcritical CO_2 (a: schematic diagram of storage tank discharge, b: *T-s* diagram of subcritical CO_2, c: the relationship between density and vapor quality, d: the relationship between density difference and vapor quality).

the density gradually decreases, and the slope of the curve (the partial derivative of density with respect to temperature, $d\rho/dx$) becomes smaller. Thus, a question arises: will changes $d\rho/dx$ in affect the expansion potential of CO_2? The result shown in Fig. 1d answers this question: with a fixed $P_{e,dis}$ of 3 MPa, the $P_{s,dis}$ of 7.3 MPa, 6.0 MPa, and 4.0 MPa were used to calculate the density changes ($\Delta\rho = \rho_{s,dis}$-$\rho_{e,dis}$) for different initial dryness levels, showing that as the dryness increases, both the value of $d\rho/dx$ and the mass of CO_2 released ($\Delta m_{CO2}=V\bullet\Delta\rho$) decrease.

Based on the above discussion, optimal storage parameters occur at the saturated liquid point ($x_{s,dis} = 0$) under subcritical conditions. When CO_2 reaches a supercritical state, the distinction between the gas and liquid phases disappears. Unlike subcritical conditions where phase transitions are characterized by vapor quality (the mass ratio of vapor to liquid), the supercritical state lacks a traditional two-phase boundary. Instead, pseudo-phase transitions are observed near the pseudo-critical

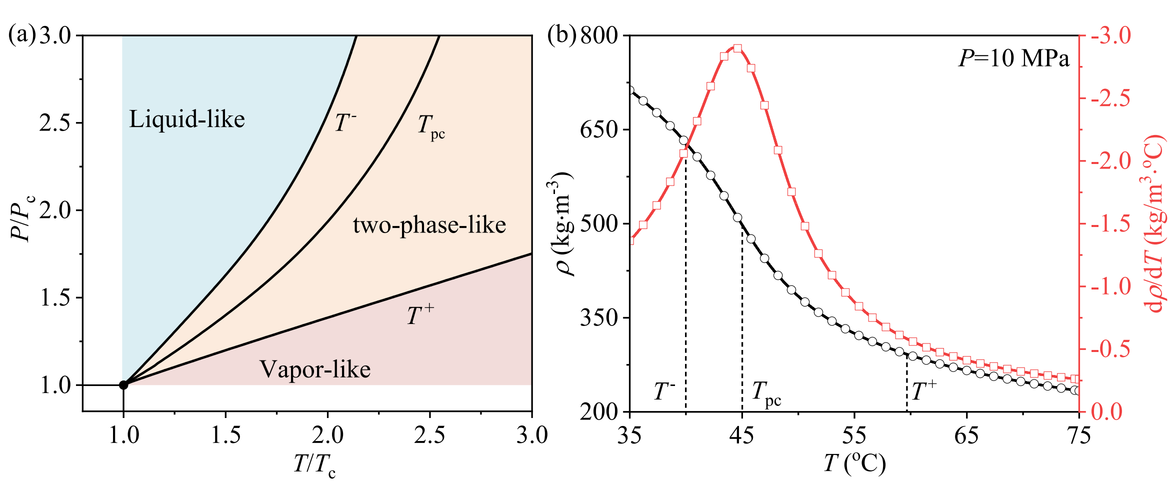

Fig. 2. The physical properties of sCO_2 near the pseudo-critical point are more similar to those at the subcritical saturation point.

temperature (T_{pc}), defined as the temperature at which the specific heat capacity reaches its maximum under a given supercritical pressure [34]. Based on T_{pc}, CO_2 can be divided into three regions (see Fig. 2a): $T < T^-$(liquid-like), $T^- < T < T^+$ (two-phase-like), $T > T^+$ (gas-like) under supercritical pressures [34]. For the CCES system, scholars have drawn an analogy between the energy release process of sCO_2 and subcritical CO_2, selecting slightly above environment temperature as storage parameters [33]. This approach aims to store sCO_2 in a liquid-like state, allowing it to expand into a gas-like state during release, thereby reducing pressure fluctuations within the storage tank.

Since the supercritical state is considered a new state rather than a simple gas or liquid, the supercritical state does not have a traditional concept of vapor quality. In the subcritical state, phase transitions are described using vapor quality, whereas in the supercritical state, pseudo-phase transitions are described using temperature. Therefore, $d\rho/dx$ can be analogous to $d\rho/dT$. Unlike the previous hypothesis, when CO_2 is in a supercritical state, the maximum value of $d\rho/dT$ occurs near the pseudo-critical point (Fig. 2b). Like the selection of subcritical CO_2 parameters, we believe that near T_{pc}, CO_2 has a stronger expansion capability. Therefore, the discharging optimization method is proposed: by selecting T_{pc} as the storage temperature, the mass of sCO_2 released can be increased.

Fig. 3 illustrates the discharge principle of the sCO_2 storage tank, with the discharging process also following isentropic conditions. At the start of discharge, the initial conditions within the tank are defined by the storage pressure $P_{s,dis}$, storage temperature $T_{s,dis}$ and storage CO_2 density $\rho_{s,dis}$. Assuming an isentropic process, the parameters at the end of discharge, including the discharge end temperature discharge end temperature $T_{e,dis}$ and $\rho_{e,dis}$ can be calculated based on the final discharge pressure $P_{e,dis}$ (see Fig. 3a and b). Fig. 3c shows that as the sCO_2 pressure increases, the pseudo-critical temperature gradually rises. When $T_{s,dis}$ is near T_{pc} temperature (T_{max}), $\Delta\rho$ reaches its maximum value (see Fig. 3d). This result is consistent with the previous inference. Since $\Delta\rho$ is nearly identical at T_{max} and T_{pc} (with the maximum difference being less than 2.2 %), T_{pc} is chosen as the design storage temperature in this study.

2.2. Introduction to the CO_2 compressed energy storage system

Fig. 4 shows the three-stage compression and three-stage expansion CCES system, which includes the compressor (C), turbine (T), high-pressure tank (HPT), cold tank (CT), hot tank (HT), and heat exchanger (HE). In addition, the system uses a low-cost flexible gas holder to store low-pressure CO_2, ensuring the working fluid remains at constant pressure and temperature. The system operates in two processes: charging and discharging. During the charging process, renewable energy generation exceeds load demand or the grid operates during off-peak hours. The CO_2 released from the gas holder is compressed to a high-pressure state through the multi-stage compressors (C1-3). The compressed heat is recovered by heat transfer fluid (thermal oil and water) released from the cold tanks (CT1-4) and stored in the hot tanks (HT1-4). The heat exchange between CO_2 and heat transfer fluid takes place in the heat exchangers (HE1-4). Finally, the high-pressure CO_2, after undergoing multiple heat exchange and compression processes, is

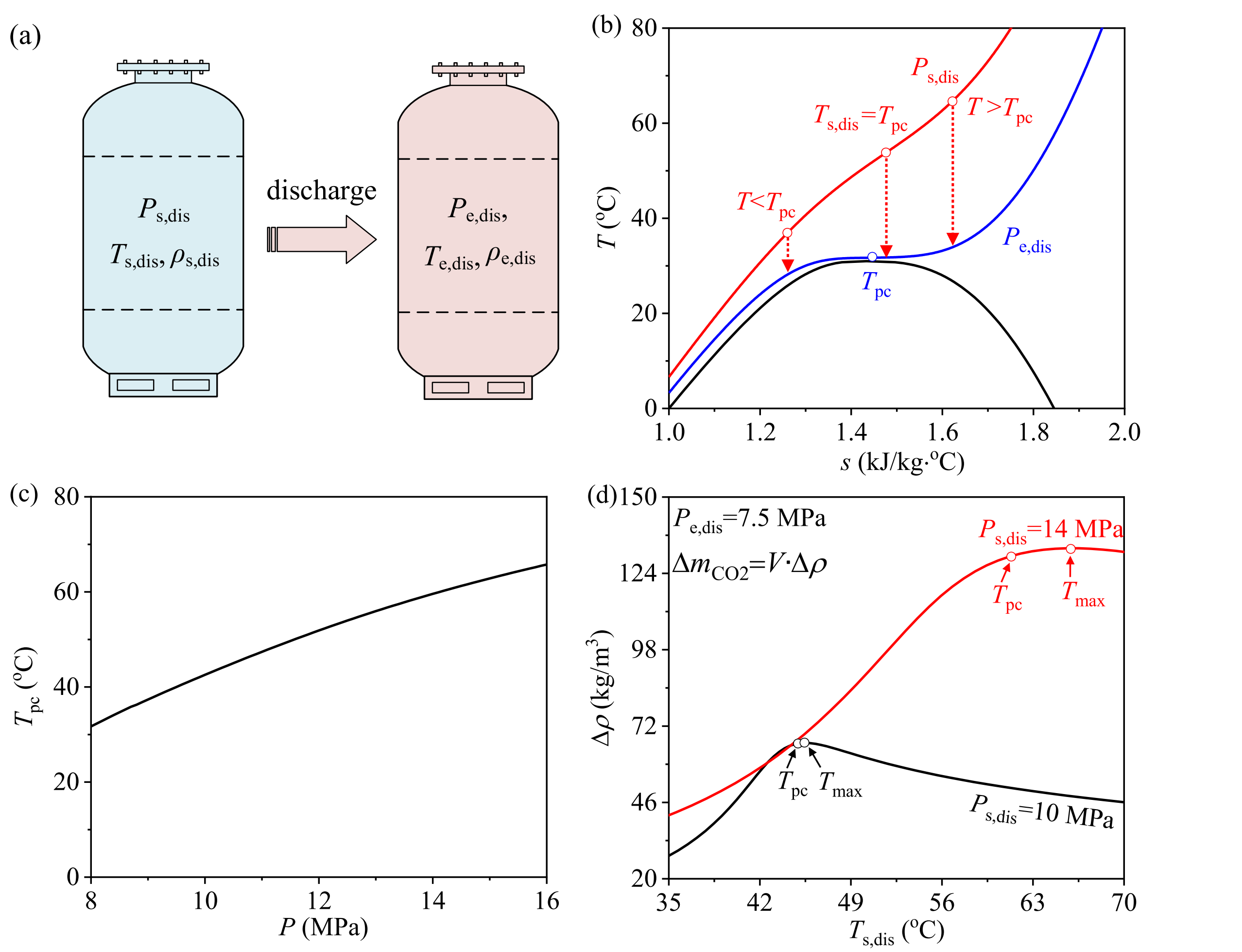

Fig. 3. Principles for selecting storage temperature of sCO_2 (a: schematic diagram of storage tank discharge, b: *T-s* diagram of sCO_2, c: the relationship between T_{pc} and pressure, d: the relationship between density difference and CO_2 storage temperature $T_{s,dis}$).

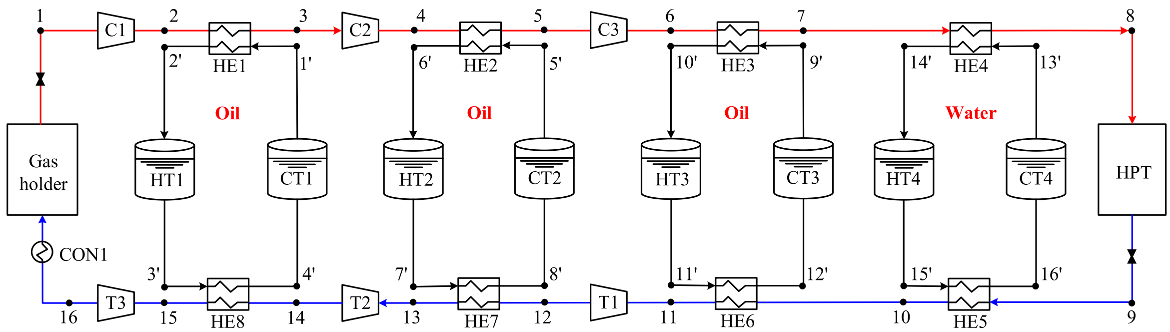

Fig. 4. Diagram of a three-stage compression and three-stage expansion CCES system.

stored in the high-pressure tank. When renewable energy generation falls below load demand or the grid operates during peak hours, the system begins the discharge process. The released high-pressure CO_2 absorbs heat from the heat transfer fluid in the hot tank and then expands through the multi-stage turbines (T1-3) to do work, driving the generator to produce electricity. Finally, the low-pressure CO_2, after releasing heat to the environment through the cooler, is stored in the gas holder, completing the discharging process. The *T-s* diagram is shown in Fig. 5.

3. Thermodynamic model

This section presents the thermodynamic models for each component, forming the foundation for the subsequent system performance analysis. The following assumptions are made to simplify the analysis.

1) Neglect heat exchange losses between components, pipelines, and the environment [36];
2) CO_2 is stored in the gas holder under ambient temperature and pressure conditions [27];
3) The mass flow rate of CO_2 remains constant and is identical during both the charging and discharging processes [37];
4) The pressure drop across the valves in the working fluid flow is neglected.

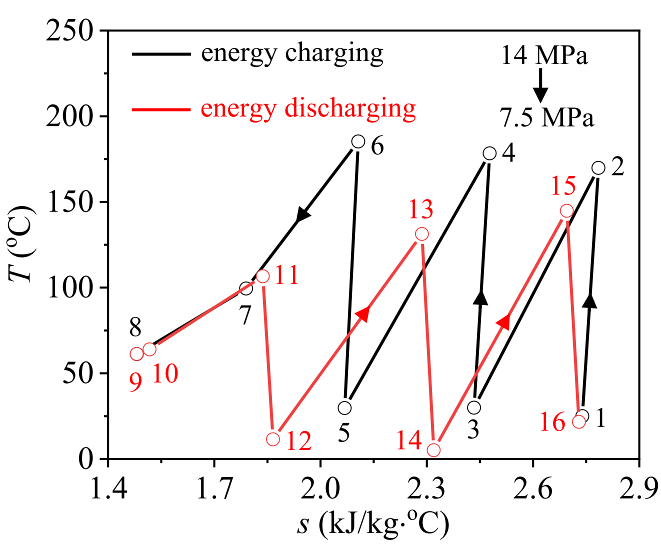

Fig. 5. *T-s* diagram of CCES system.

3.1. Component models

The key component models of the CCES system are developed based on the first law of thermodynamics and the law of mass conservation. The mathematical representation of the component models is as follows.

(1) compressor

During the charging process, CO_2 at the initial pressure passes through compressors C1 and C2 to reach an intermediate pressure and then enters C3 to be compressed to the final pressure. The compression ratios π of the three compression stages are equal. The compressor energy consumption E_C during the charging process can be expressed as [38]:

$$E_C = \int_{t_{s,char}}^{t_{e,char}} m_{CO2}\left(h_{out,C} - h_{in,C}\right)dt = \int_{t_{s,char}}^{t_{e,char}} W_C dt \tag{1}$$

Where W is the power rate, m is the mass flow rate, h is the specific enthalpy, and t is time. The subscript C refers to the compressor, s denotes the start, e denotes the end, and char refers to the charging.

The isentropic efficiency of the compressor varies with changes in basic operating parameters such as speed and mass flow rate. The off-design performance of the compressor is obtained from the compressor characteristic map [39,40], and its mathematical fitting formula expression is [41]:

$$\frac{\eta_{C,od}}{\eta_{C,d}} = \left[1 - 0.3(1 - N_{re})^2\right]\left(\frac{N_{re}}{m_{re}}\right)\left(2 - \frac{N_{re}}{m_{re}}\right) \tag{2}$$

Where N is the rotational speed, the subscript d denotes design conditions, od denotes off-design conditions, and re represents the corrected relative value. The expression for the corrected relative speed N_{re} is as follows:

$$N_{re} = \frac{N_{od}}{N_d}\sqrt{\frac{T_{in,d}}{T_{in,od}}} \tag{3}$$

Where T is the temperature. The expression for the corrected relative mass flow rate m_{re} is:

$$m_{re} = \frac{m_{od}P_{od}}{m_d P_d}\sqrt{\frac{T_{in,od}}{T_{in,d}}} \tag{4}$$

The relationship between the compression ratios π and the m_{re} is as follows:

$$\frac{\pi_{od}}{\pi_d} = C_1 m_{re}^2 + C_2 m_{re} + C_3 \tag{5}$$

Where C_1, C_2 and C_3 are the fitted empirical coefficients, and their expressions are as follows:

$$C_1 = N_{re} \, / \, \left[p(1 - q \, / \, N_{re}) + N_{re}(N_{re} - q)^2\right] \quad (6)$$

$$C_2 = (p - 2qN_{re}) \, / \, \left[p(1 - q \, / \, N_{re}) + N_{re}(N_{re} - q)^2\right] \quad (7)$$

$$C_3 = -\left(pqN_{re} - q^2 N_{re}^3\right) \, / \, \left[p(1 - q \, / \, N_{re}) + N_{re}(N_{re} - q)^2\right] \quad (8)$$

Where p and q are empirical constants. For axial compressors, p and q are set to 0.36 and 1.06 [40], respectively. As shown in Fig. 6. When the relative speed is constant, as the relative mass flow rate decreases, the relative pressure ratio gradually increases, while the isentropic efficiency gradually decreases.

(2) turbine

During the discharging process, CO_2 expands in three stages with each stage applying the same expansion ratio (the ratio of inlet pressure to outlet pressure), maintaining consistent thermodynamic behavior across all turbines. The expression for the turbine output energy E_T is given by Ref. [38]:

$$E_T = \int_{t_{s,dis}}^{t_{e,dis}} m_{CO2}\left(h_{in,T} - h_{out,T}\right) dt = \int_{t_{s,dis}}^{t_{e,dis}} W_T dt \quad (9)$$

To analyze the impact of off-design conditions on turbine performance, the relationship between isentropic efficiency and expansion ratio referenced from literature [37,42] is used. The calculation expression for isentropic efficiency is as follows:

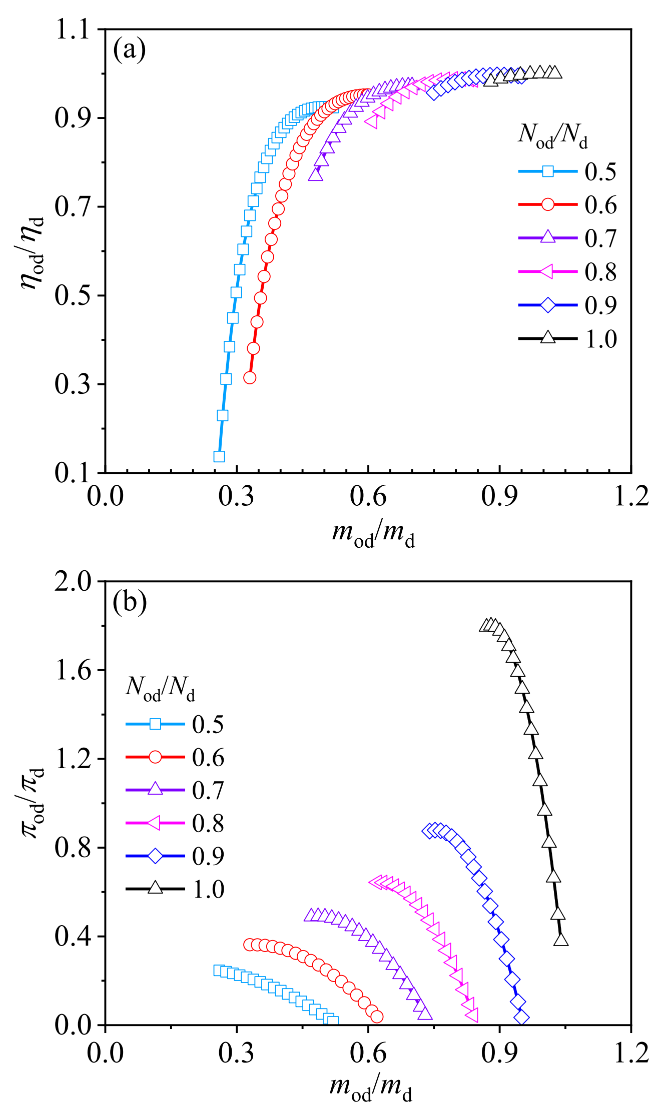

Fig. 6. Performance curve of the compressor under off-design conditions.

$$\eta_T = 0.0269\left(\frac{P_{in,T}}{P_{out,T}}\right) + 0.7501 \quad (10)$$

Where P is pressure.

(3) High-pressure tank (HPT)

The HPT model is established based on the principles of energy conservation and mass conservation. Its expression is as follows [43]:

$$\frac{dm_{HPT}}{dt} = m_{CO2,in} - m_{CO2,out} \quad (11)$$

$$\frac{d(mu)_{HPT}}{dt} = m_{CO2,in} h_{CO2,in} - m_{CO2,out} h_{CO2,out} \quad (12)$$

Where u represents the specific internal energy of CO_2 in the HPT.

(4) Hot tank (HT) and Cold tank (CT)

During the charging process, the heat transfer fluid released from the cold tank absorbs the compressed heat and then stores it in the hot tank. In the discharging process, the hot fluid released from the hot tank transfers heat to the CO_2, after which it returns to the cold tank. The system consists of four hot tanks and four cold tanks, with the working fluid in HT4 and CT4 being water, while the remaining tanks contain thermal oil. The models for the cold tanks and hot tanks are both based on the principles of energy and mass conservation [44]:

$$\frac{dm_T}{dt} = m_{htf,in} - m_{htf,out} \quad (13)$$

$$\frac{d(mu)_T}{dt} = m_{htf,in} h_{htf,in} - m_{htf,out} h_{htf,out} \quad (14)$$

Where the subscript htf represents the heat transfer fluid.

(5) Heat exchanger

Due to the significant variations in CO_2 properties during heat exchange, the heat exchanger is divided into multiple sub-heat exchangers instead of being modeled using the logarithmic mean temperature difference method [38]. The energy balance equation inside the heat exchanger is presented below [37,43]:

$$Q_{HE} = \sum_{i=1}^{N} Q_{HE,i} \quad (15)$$

$$Q_{HE,i} = m_{CO2}\left(h_{CO2,i+1} - h_{CO2,i}\right) = m_{htf}\left(h_{htf,i+1} - h_{htf,i}\right) \quad (16)$$

3.2. Evaluation criteria

To more effectively evaluate the performance characteristics of CCES system, the following indicators are introduced: total output energy (E_T), total discharge mass (Δm_{dis}), round trip efficiency(η_{RTE}) and energy storage density (ESD). Their expressions are presented below [27,45,46]:

$$E_T = \int_{t_{s,dis}}^{t_{e,dis}} (W_{T1} + W_{T2} + W_{T3}) dt \quad (17)$$

$$\Delta m_{dis} = \int_{t_{s,dis}}^{t_{e,dis}} m_{CO2} dt \quad (18)$$

$$\eta_{RTE} = \frac{\int_{t_{s,dis}}^{t_{e,dis}} (W_{T1} + W_{T2} + W_{T3})dt}{\int_{t_{s,char}}^{t_{e,char}} (W_{C1} + W_{C2} + W_{C3})dt} \tag{19}$$

$$ESD = \frac{\int_{t_{s,dis}}^{t_{e,dis}} (W_{T1} + W_{T2} + W_{T3})dt}{V_{HPT}} \tag{20}$$

3.3. Model validation

Based on the above component models, the system model is established in Dymola using the Modelica language. Due to the difficulty in finding a similar CCES system in existing experiments, the accuracy of the system components is validated by referencing simulation model results from the literature. The heat exchanger and storage tank models are referenced from the literature [37], and Fig. 7a shows the CCES system diagram. The comparison results of models are shown in Fig. 7b–e. The maximum relative error between the simulation and literature results is 1.37 %, which is within an acceptable range. Additionally, the comparison between the compressor and turbine results and those from the literature [47] is shown in Table 1. The results

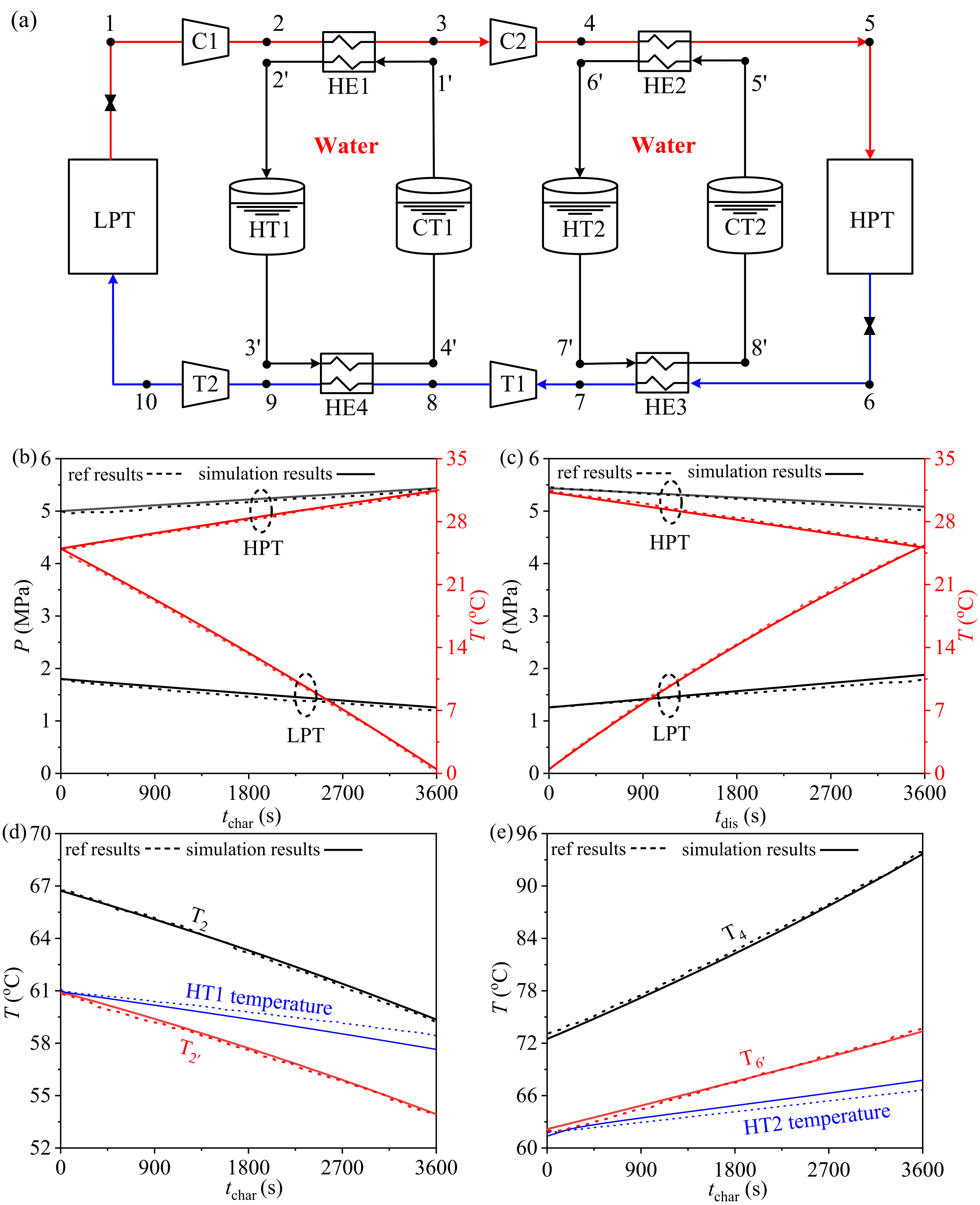

Fig. 7. Comparison diagram of simulation results and literature data (a: the CCES system from the literature [37], b: comparison diagram of high-pressure tank HPT and low-pressure tank LPT during the charging process, c: comparison diagram of HPT and LPT during the discharging process, d: Comparison diagram of HE1 and HT1, e: Comparison diagram of HE2 and HT2).

Table 1
Verification of compressor and turbine.

Components	Ref [47]		Simulation	Relative error (%)
	Inlet parameters	Output parameters	Output parameters	
Compressor	28.36 °C (T_{in}), 2.97 MPa (P_{in}), 14.85 MPa (P_{out})	184.03 °C (T_{out})	178.87 °C (T_{out})	2.8
Turbine	122.75 °C (T_{in}), 14.41 MPa (P_{in}), 6.62 MPa (P_{out})	59.51 °C (T_{out})	60.55 °C (T_{out})	1.75

indicate that the maximum relative error is 1.11 %. Therefore, these models can be used for subsequent simulation calculations.

3.4. Control and methods

The initial temperature ($T_{s,char}$) of the HPT during the charging process is determined through simulation calculations. Under the conditions of the final storage pressure, temperature, initial pressure, and mass flow rate of CO_2 ($P_{e,char}$, $T_{e,char}$, $P_{s,char}$, m_{CO2}), the initial temperature of HPT can be calculated.

The control process of CCES system is divided into the charging process and the discharging process. As shown in Fig. 8a, during the charging phase, the pressure and temperature of the HPT continuously change over time. This means that the compressor must adjust its speed to ensure that the inlet CO_2 pressure of the HPT ($P_{HPT,in}$) is always greater than the CO_2 pressure inside the HPT (P_{HPT}). When the CO_2 pressure inside the HPT reaches the maximum set pressure value ($P_{HPT} = P_{s,char}$), the charging process ends. $T_{C,in}$ and $T_{HPT,in}$ are controlled by heat exchanger flow. The outlet CO_2 temperature of the heat exchanger ($T_{HE,out,d}$) is set. If the actual outlet temperature ($T_{HE,out,od}$) does not match this set value, adjustments will be made by modifying the flow rate of the heat transfer fluid ($m_{htf,in}$) accordingly.

The control logic for the discharging process is illustrated in Fig. 8b. The initial parameters of the CO_2 in the HPT and hot tank during the discharge process are obtained from the simulation results of the charging system. Since the pressure of the gas holder (P_{GH}) is set at 0.1 MPa and the release pressure of the HPT varies with time, it is necessary to adjust the expansion ratio (π') of the turbine to ensure that the exit pressure of the third turbine (T3) is greater than P_{GH}. The mass flow rate of the heat transfer fluid (m_{htf}) is taken as the average mass flow rate. If the turbine outlet temperature is lower than the liquefaction temperature, then the mass flow rate of the heat transfer fluid (m_{htf}) needs to be adjusted. The discharging process ends when the pressure of the working fluid in the high-pressure tank equals the minimum set pressure ($P_{HPT} = P_{e,char}$).

4. Results and discussion

4.1. System performance under design conditions

The main design parameters of the CCES system are shown in Table 2. The pressure range of the HPT is 14.0 to 7.5 MPa, with a storage temperature of 61.3 °C $T_{s,dis}$. The volume of the HPT is 23734.4 m^3. The function of the low-pressure gas holder is to maintain the CO_2 parameters equal to the ambient conditions. The rated charging power is 100.0 MW. The charging time is consistent with the discharging time,

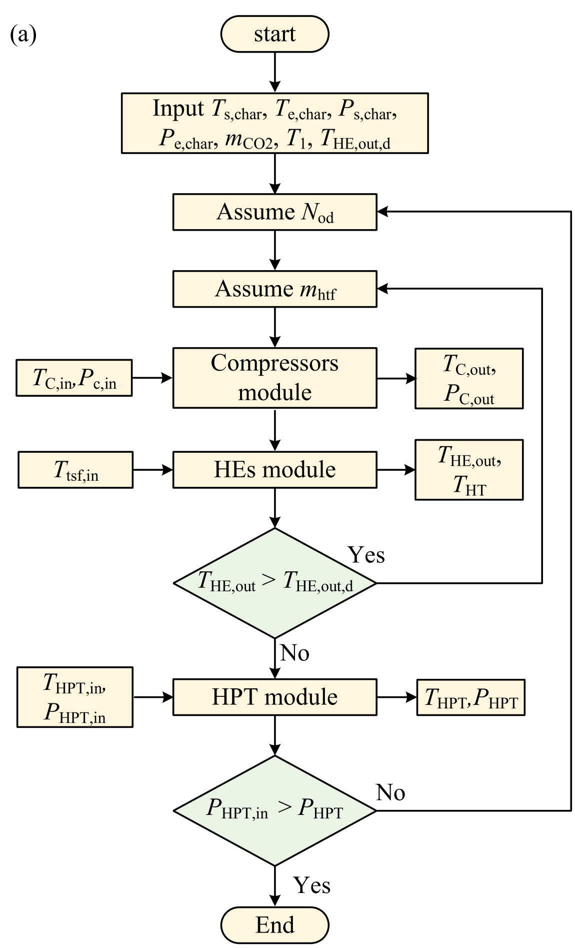

Fig. 8. System simulation logic diagram (a: charging process, b: discharging process).

Table 2
Main design parameters of the CCES.

parameters	value
Charging time/discharging time	3.00 h
Compression power consumption W_C	100.00 MW
Environmental temperature	25 °C [49]
Environmental pressure	0.1 MPa [49]
CO_2 storage pressure $P_{s,dis}$	14.00 MPa
CO_2 storage temperature $T_{s,dis}$	61.25 °C
CO_2 storage pressure at the end of discharging $P_{e,dis}$	7.50 MPa
CO_2 mass flow rate during the charging/discharging process	285 kg/s
CO_2 pressure in gas holder	0.1 MPa
CO_2 temperature in gas holder	25 °C
Isentropic efficiency of Compressor	85 % [38]
Heat exchanger pinch point temperature difference	5 °C [50]
Heat exchanger pressure drop loss	1 %
Cold tank outlet temperature (CT1, CT2, CT4)	20 °C
Cold tank outlet temperature (CT3)	80 °C
Design volume of the HPT	23734.35 m^3

both lasting 3 h. The mass flow rate of CO_2 remains at 285.0 kg/s the outlet temperatures of CT1, CT2, CT4 are 20 °C, while the outlet temperature of CT3 is set to 80 °C. Based on the above parameters, the performance characteristics of the components and system during the charging and discharging process will be discussed in the following sections.

4.1.1. Key parameters change during the charging process

The dynamic variations in the compressor pressure ratio π_{od} during the charging process (see Fig. 9a) are inherently governed by the thermodynamic constraints of the CCES system. The progressive increase in π_{od} (4.53–5.37) reflects the increased work input required to compress CO_2 into the supercritical regime. This elevated compressor power consumption enhances heat recovery efficacy. Then, the temperature of cooling fluid will rise (see Fig. 9b and c).

The heat exchanger network (HE1-4) is designed to exploit the unique thermodynamic behavior of sCO_2. In HE3 (see Fig. 9d), the sharp rise in thermal oil outlet temperature (T_{10}: 158.3 °C–174.7 °C) is related to the change of compressor pressure ratio. Here, the thermal oil inlet temperature ($T_{9'} = 80$ °C) is strategically maintained above the pseudo-critical temperature to enhance heat transfer efficiency. This approach minimizes entropy generation during heat recovery by avoiding the high specific heat capacity of sCO_2 near the T_{pc}.

Conversely, HE4 (see Fig. 9e) operates near the pseudo-critical region, where the specific heat capacity of sCO_2 varies sharply with temperature. The gradual increase in cooling water temperature (46.2 °C–90.7 °C) indicates inefficient heat transfer in this region. Throughout the charging process, the HPT storage pressure rises from 7.5 MPa to 14 MPa, and the storage temperature increases from 31.8 °C to 61.3 °C (see Fig. 9f).

4.1.2. Key parameters change during the discharging process

For the discharging process, the parameter changes of the CO_2 in HPT are shown in Fig. 10a. Due to the continuously decreasing outlet pressure of HPT, the turbine expansion ratio π' must also be reduced to maintain the CO_2 inlet pressure of the gas holder at 0.1 MPa. As shown in Fig. 10b, π' decreases from 5.2 to 4.2.

As the outlet CO_2 temperature of the HPT steadily decreases and is affected by near-critical properties, the heat transfer temperature differences in HE5 and HE6 become the higher, measuring 23.2 °C and 54.1 °C, respectively (see Fig. 10c and d). The inlet CO_2 temperature of HE7-8 is gradually increasing, and the outlet CO_2 temperature rises accordingly (see Fig. 10e and f), which is due to the continuous decrease in CO_2 pressure.

4.1.3. Performance variations of CCES system

Under the design conditions, the variations in system power consumption and expansion work are shown in Fig. 11a. With the same compression ratio, the C1-2 compression power consumption is relatively high, while that of C3 is lower due to exceeding the supercritical pressure. Due to the lower inlet temperature at T1 (T_{11}), the expansion work W_{T1} is smaller than W_{T2} and W_{T3}. Fig. 11b shows a comparison of total compression consumption W_C and expansion work W_T, along with the round-trip efficiency η_{RT}. The W_C increases from 93.2 MW to 107 MW as the compression ratio rises, while the W_T decreases from 72.2 MW to 66.2 MW as the expansion ratio decreases. The η_{RT} drops from 77.1 % to 61.67 %. The average compression power consumption $W_{C,ave}$ is 100.0 MW, the average expansion power $W_{T,ave}$ is 69.1 MW, and the average round-trip efficiency $\eta_{RT,ave}$ is 69.3 %.

4.2. The effect of different HPT parameters on the system

As discussed in section 2, the discharging time of sCO_2 HPT is related to the storage temperature $T_{s,dis}$. When the $T_{s,dis}$ is near the T_{pc}, the expansion potential of sCO_2 within the tank reaches its peak, allowing for the release of the maximum mass of CO_2. Building on this principle, a novel CCES system design is proposed in this study, leveraging the unique characteristics of sCO_2 HPT.

Fig. 12a and b shows the changes in temperature of HPT with discharging time. The results indicate that when the $T_{s,dis}$ deviates significantly from the T_{pc}, the discharging time decreases (when $T_{s,dis}$ is 35.0, 61.3, 75.0 °C, t_{dis} are 0.96, 3.00, 2.94 h). Fig. 12c shows the variation of expansion work overtime. As the discharging process progresses, the outlet CO_2 temperature and pressure from the HPT continuously decrease. Consequently, the expansion capability of CO_2 gradually diminishes, that is, W_T gradually decreases. The η_{RT} shows a similar trend.

As shown in Fig. 13a, the discharging time (t_{dis}) exhibits a parabolic dependence on storage temperature ($T_{s.dis}$), peaking near the pseudo-critical temperature at both 10 MPa ($T_{pc} = 45.0$ °C) and 14 MPa ($T_{pc} = 61.3$ °C). This is because sCO_2 has the strongest expansion capability near the T_{pc}, which extends the discharging time. At pressures of 10 and 14 MPa, the discharging times (t_{dis}) are as follows: 1.53 h (10 MPa, T_{pc}), 1.53 h (10 MPa, T_{max}), 3.00 h (14 MPa, T_{pc}), and 3.03 h (14 MPa, T_{max}). It can be observed that t_{dis} is very close when $T_{s,dis}$ equals T_{pc} and T_{max}, with a maximum difference of only 2 %. At $T_{s,dis} = T_{max}$, sCO_2 achieves an optimal balance between liquid-like density and gas-like compressibility, enabling maximization of *ESD* and E_T. Deviations from T_{max} disrupt this equilibrium: when $T_{s,dis}$ increase from $T_{s,dis} = 35$ °C to T_{max}, the E_T increases from 40.74 MW to 101.60 MW ($P_{s,dis} = 10$ MPa) and from 64.27 MW to 215.84 MW ($P_{s,dis} = 14$ MPa), while the *ESD* rises from 1.72 kWh/m^3 to 4.28 kWh/m^3 and from 2.71 kWh/m^3 to 9.10 kWh/m^3 (see Fig. 13b and c).

The η_{RT} follows a distinct trend, improving monotonically with $T_{s,dis}$ but exhibiting steepest gains near T_{pc} (see Fig. 13d). This nonlinearity arises from the temperature-dependent effectiveness of heat recovery during compression. At $T_{s,dis} < T_{pc}$, liquid-like state amplifies thermal resistance in heat exchangers. Above T_{pc}, the gas-like behavior of sCO_2 lowers thermal resistance. The phenomenon can be analyzed using the average heat transfer temperature difference (ΔT_{ave}) of the heat exchange system, which can be expressed as follows:

$$\Delta T_{ave} = \int_{t_s}^{t_e} \frac{(T_2 - T_{15}) + (T_4 - T_{13}) + (T_6 - T_{11})}{3} dt \tag{21}$$

Pressure further affects the heat transfer performance. As the temperature increases, the ΔT_{ave} at $P_{s,dis} = 14$ MPa gradually exceeds that at $P_{s,dis} = 10$ MPa. (see Fig. 14). This characteristic is consistent with the trend of round-trip efficiency variation shown in Fig. 13d.

To analyze the impact of sCO_2 parameter selection at the system level, the total energy release during the discharging process (E_{dis}) is introduced as a key metric to evaluate the work extraction capacity of CO_2, reflecting its thermodynamic efficiency. It can be expressed as follows:

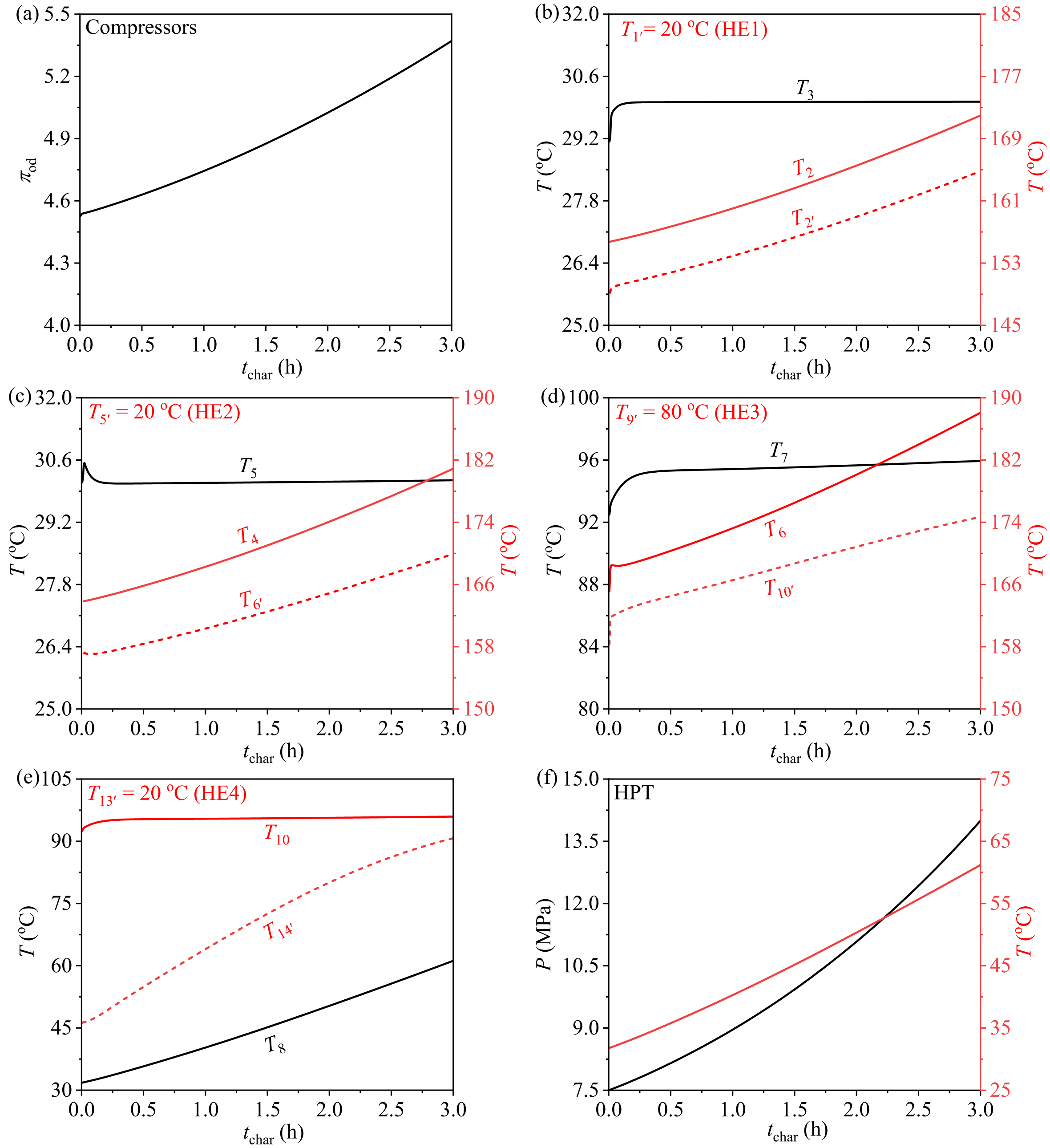

Fig. 9. Parameter variations of key components during the charging process.

$$E_{dis} = \Delta E_{HPT} + Q_{HE} - Q_{release} = \int_{t_{s,dis}}^{t_{e,dis}} W_{dis} dt \tag{22}$$

$$E_T = \int_{t_{s,dis}}^{t_{e,dis}} W_{dis} \cdot \eta_T dt \tag{23}$$

Where, ΔE_{HPT} represents the change in energy in the HPT, Q_{HE} is the heat transfer amount in heat exchangers, $Q_{release}$ represents the heat released to the environment under ideal conditions. As the storage temperature approaches T_{pc}, not only does the discharging time prolong, but the energy output capacity of CO_2 is also significantly enhanced (see Fig. 15). Thus, this result offers a foundational rationale for selecting the temperature near the T_{pc} as the optimized storage temperature.

Fig. 16 presents a 2D contour plot illustrating the impact of CO_2 storage parameters on system performance. The results indicate that the t_{dis}, Δm_{CO2} and W_T are positively correlated with the proximity of $T_{s,dis}$ to the T_{pc} and the $P_{s,dis}$. The η_{RT} is delineated by the T_{pc} line. Below T_{pc}, pressure exhibits a positive correlation with η_{RT}, whereas above it, the correlation becomes negative. It is worth noting that when the temperature is above the T_{pc}, a higher pressure actually leads to lower η_{RT}. This phenomenon arises from the fact that low-pressure sCO_2 exhibits properties more characteristic of a gas when operating above the T_{pc} [34]. This behavior enhances its heat transfer effectiveness with the heat transfer fluid. Consequently, η_{RT} is improved.

4.3. Comparative advantages of proposed CCES system

By optimizing storage parameters based on our proposed criteria, we have achieved a significant performance improvement in CCES system. To highlight the performance advantages of the proposed system, a comparison is made with several common compressed gas energy storage systems [37,48]. The focus of this study is mainly on the HPT

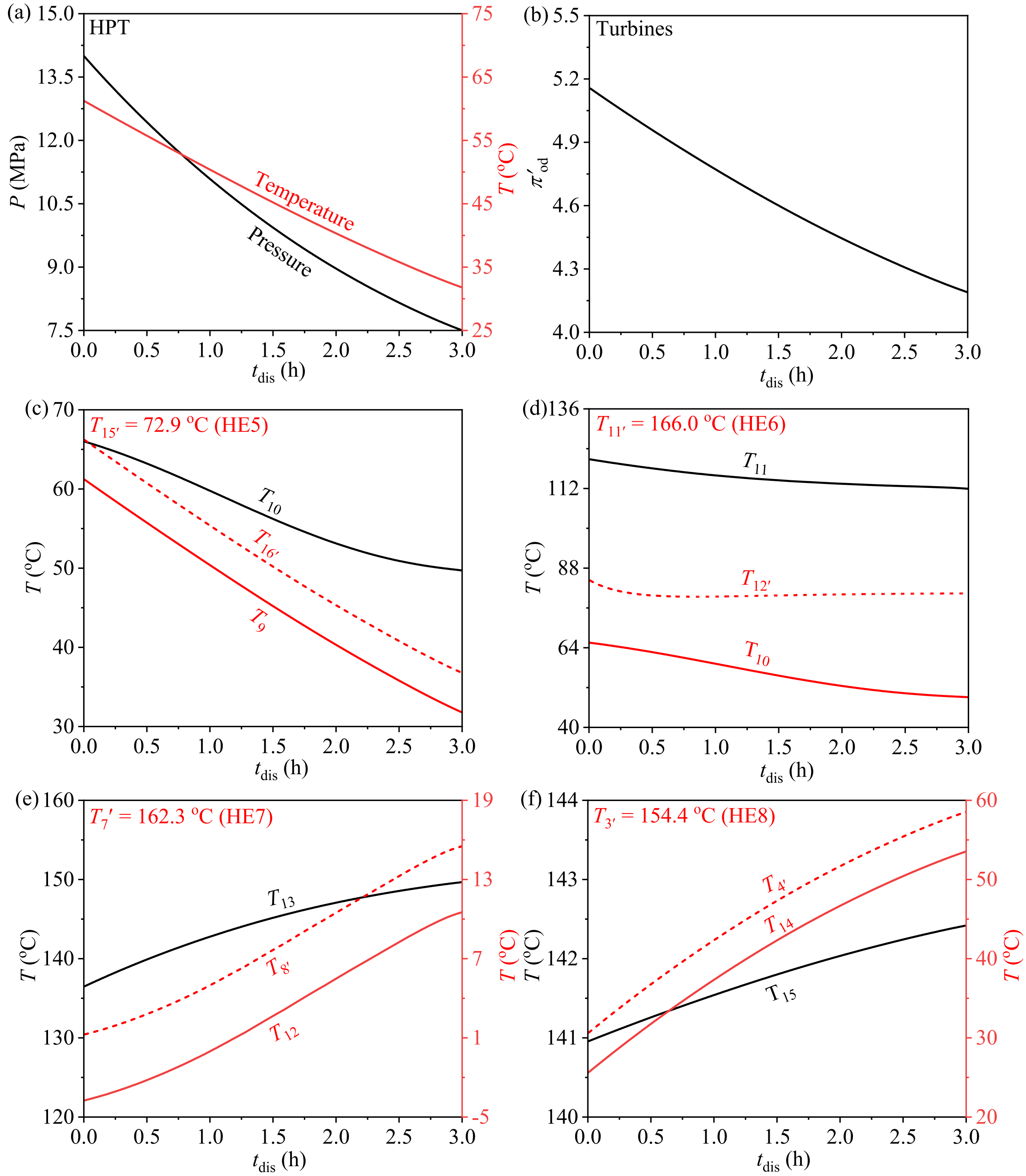

Fig. 10. Parameter variations of key components during the discharging process.

parameter. Therefore, the mass storage density of the HPT (β_{HPT}) is proposed to measure the difference in the energy storage efficiency of system:

$$\beta_{HPT} = \int_{t_{s,dis}}^{t_{e,dis}} m_{CO2}dt \Big/ V_{HPT} \tag{24}$$

The main parameters of different systems are shown in Table 3. The comparison of the mass storage density and round-trip efficiency of three systems is shown in Fig. 17. The optimized CCES system exhibits a significantly higher mass density than literature values [37,48], consistent with its enhanced energy storage density. Additionally, the higher CO_2 storage temperature of the proposed system results in improved round-trip efficiency, surpassing the two references system by 5.03 % and 3.06 %, respectively. This comparative analysis conclusively demonstrates the marked superiority of the optimized CCES system over conventional configurations, achieving comprehensive performance enhancements in both energy storage density and round-trip efficiency critical for practical large-scale deployment.

4.4. Economic analysis

Economic analysis serves as an important reference for evaluating the performance of a system. Table 4 presents the economic parameters of the system. Furthermore, levelized cost of electricity (*LCOE*) is introduced in this study to assess the overall economic benefits of the CCES system, which can be expressed as follows:

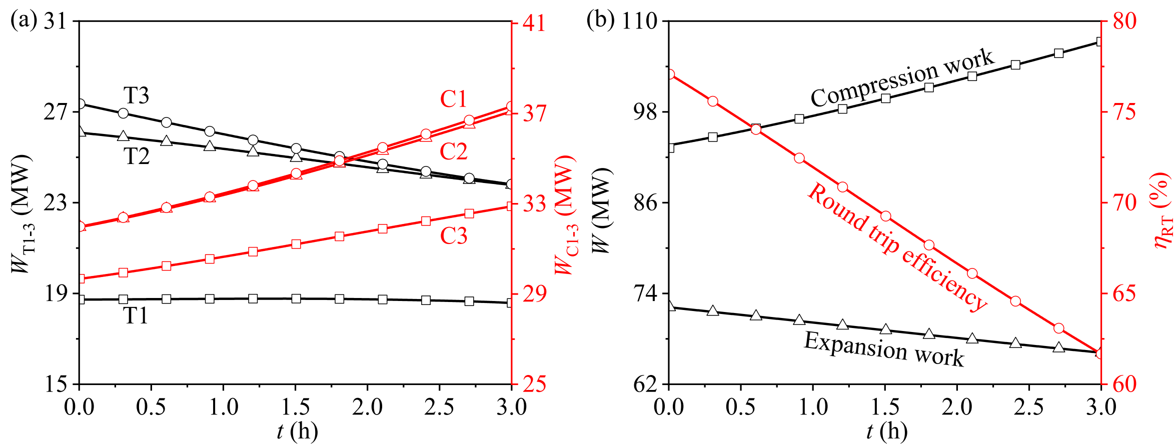

Fig. 11. System performance diagram under designed conditions (a: diagram of system compression work and expansion work variations, b: diagram of variations in system power consumption, power output, and round-trip efficiency).

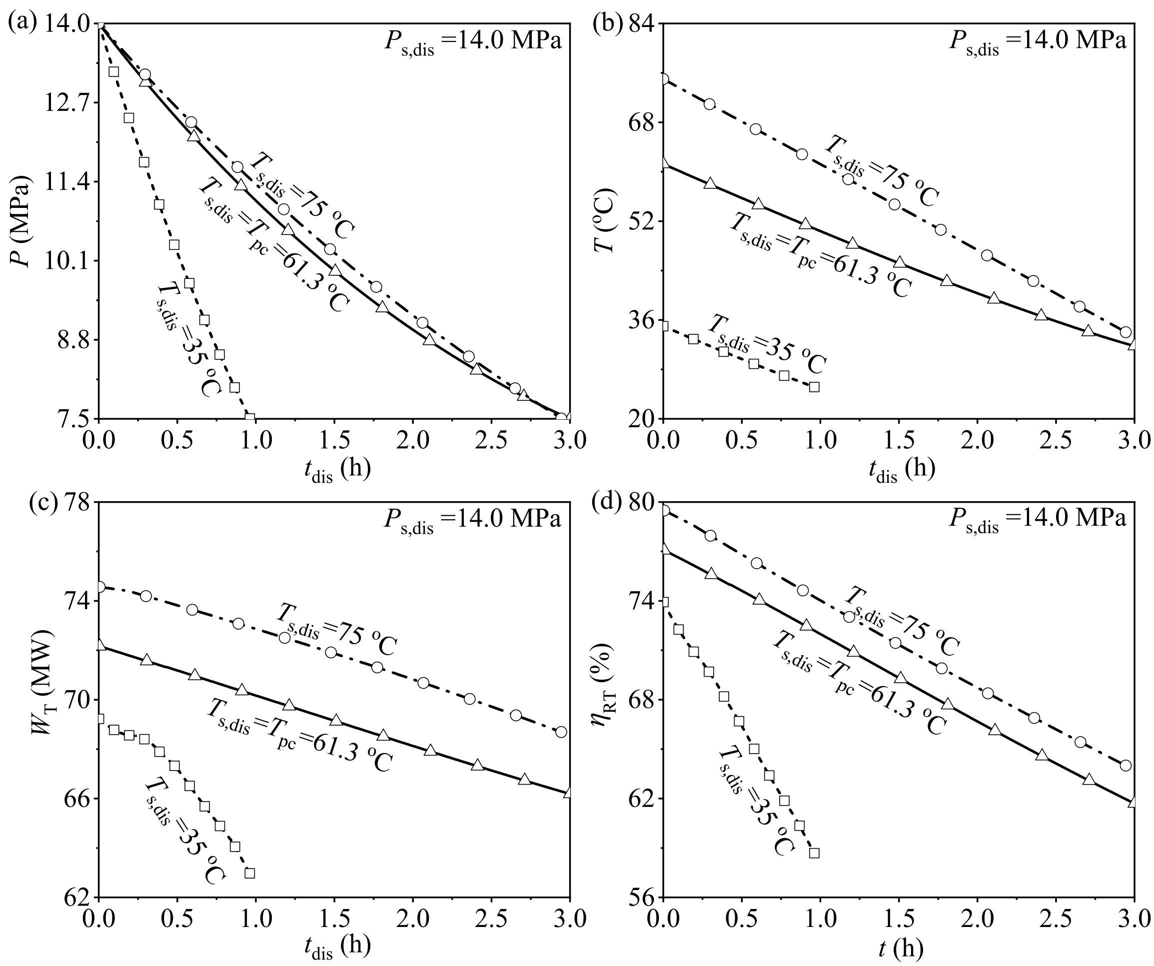

Fig. 12. Diagram of the variation in key system performance indicators over time (a–b: the relationship between pressure and temperature variations of the HPT over time, c: the relationship between turbine output power and time, d: the relationship between round-trip efficiency and time).

$$LCOE = \frac{Z_{tot} + \sum_{y=1}^{N} \frac{Z_{OM}+Z_{elec}}{(1+Ir)^y}}{\sum_{y=1}^{N} \frac{n \cdot \int_{t_{s,dis}}^{t_{e,dis}} W_T dt}{(1+Ir)^y}} \tag{25}$$

Where, Z_{tot} represents the initial capital investment cost of the equipment, and the key component cost models are shown in Table 5. N denotes the operational lifetime in years, n represents the number of cycles, and Ir is the interest rate. The operation and maintenance cost Z_{OM} and the total charging electricity cost $Z_{elec,v}$ can be expressed as follows:

$$Z_{OM} = 0.06 Z_{tot} \tag{26}$$

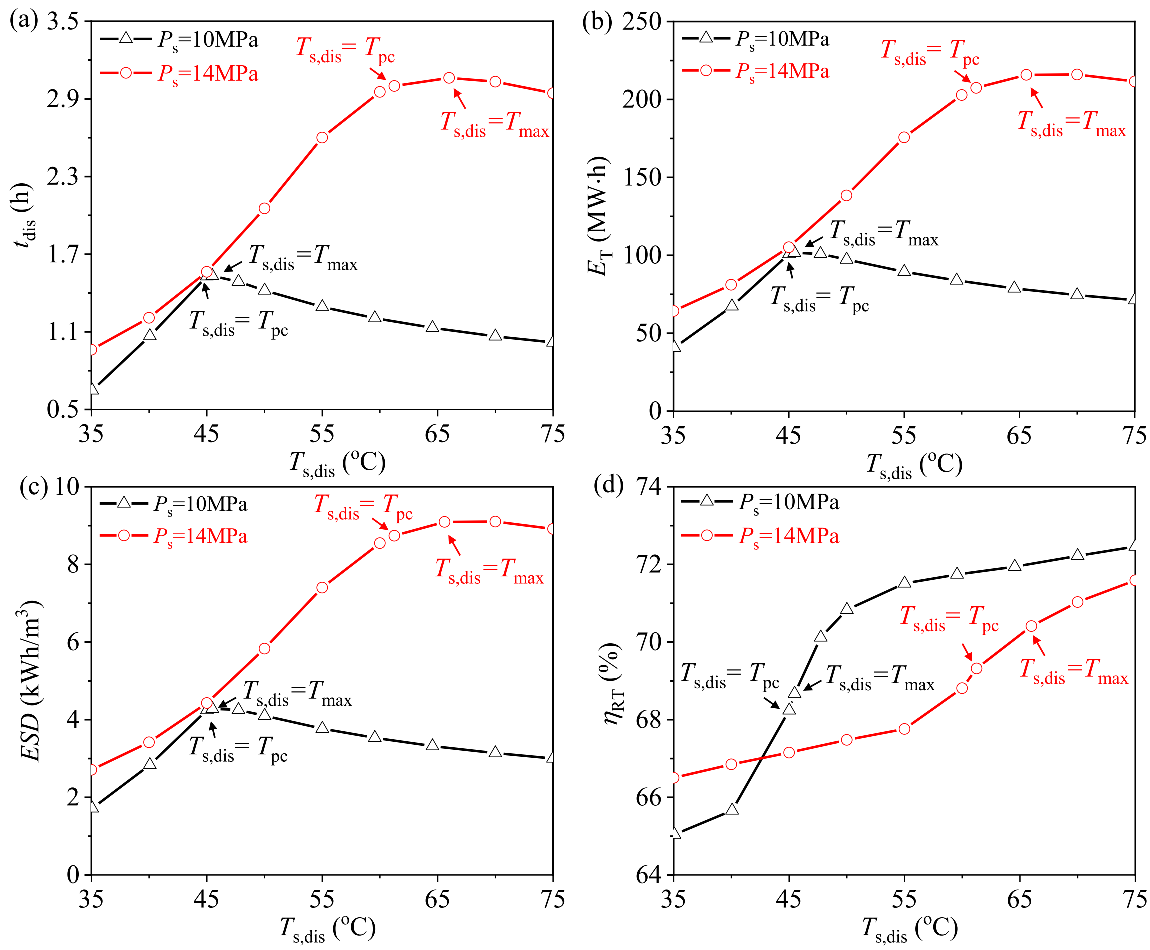

Fig. 13. Diagram of system performance variations under different gas storage parameters (a: the relationship between t_{dis} and CO_2 storage parameters, b: the relationship between E_T and CO_2 storage parameters, c: the relationship between *ESD* and CO_2 storage parameters, d: the relationship between η_{RT} and CO_2 storage parameters).

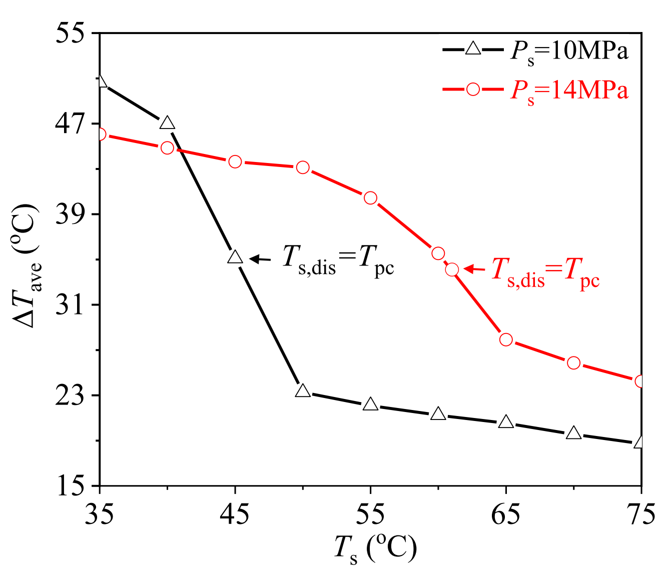

Fig. 14. The impact of different gas storage parameters on the average heat exchange temperature difference.

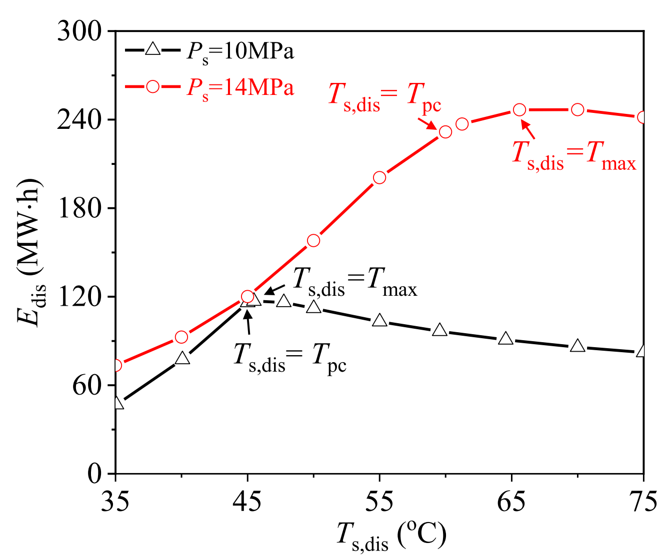

Fig. 15. The relationship between total energy and storage parameter during the discharging process.

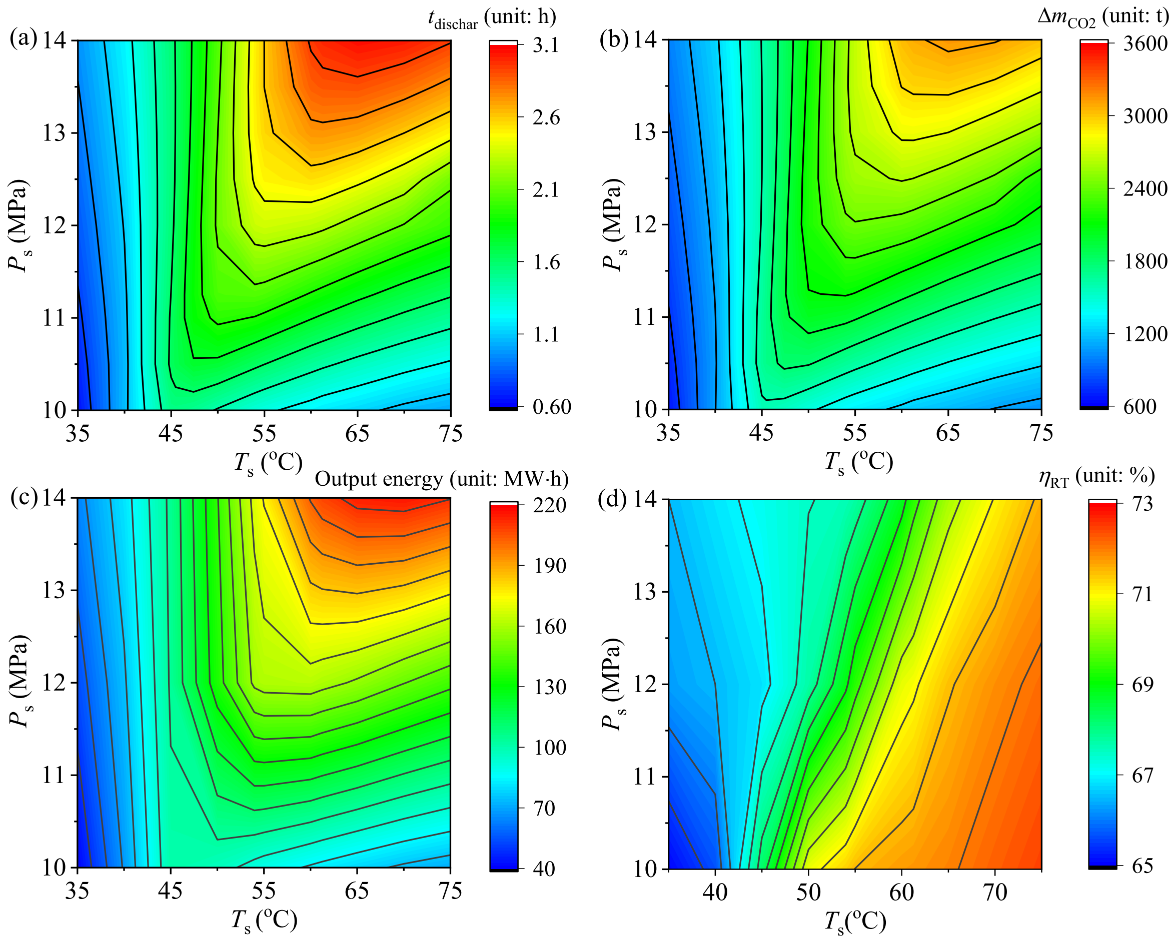

Fig. 16. 2D contour plot on system performance (a: discharging time lines, b: discharging mass lines, c: output energy lines, d: round-trip efficiency lines).

Table 3
Main parameters of systems.

Parameter	Proposed system	CCES [37]	CAES [48]
Maximum pressure of HPT (MPa)	14.0	5.4	15
Minimum pressure of HPT (MPa)	7.5	5.0	10
Working fluid flow rate (kg/s)	285.0	24	50
Discharging time (h)	3.0	1	3.8
HPT volume (m^3)	23734.4	10000	20000
Isentropic efficiency of compressors (%)	85.0	75.8	86.7
Isentropic efficiency of turbines (%)	89.0	83.1	92
Energy storage density (kWh/m^3)	8.7	0.06	4.3

$$Z_{elec,v} = z_{elec,v} \cdot n \cdot \int_{t_{s,char}}^{t_{e,char}} W_C dt \tag{27}$$

Where, $z_{elec,v}$ denotes the charging electricity price.

Net present value (*NPV*) is an important indicator used to evaluate the overall profitability of the CCES system. It can be calculated as follows:

$$NPV = \sum_{y=1}^{N} \frac{Z_{elec,p} - Z_{OM} - Z_{elec,v}}{(1 + Ir)^y} - Z_{tot} \tag{28}$$

Where $Z_{elec,p}$ is the total revenue from discharging, which can be expressed as follows:

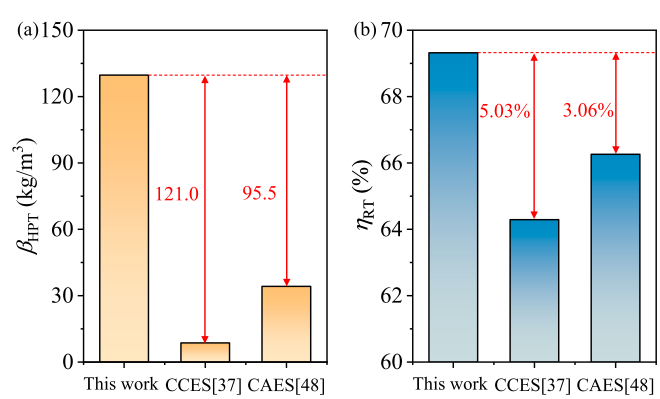

Fig. 17. Comparative analysis between optimized system and reference systems (a: comparison of mass storage density, b: comparison of round-trip efficiency).

Table 4
System economic parameter [27].

Parameter	Value	Unit
Charging electricity price	0.052	$/kWh
Discharging electricity price	0.203	$/kWh
Operating life	30	Year
Operating cycles per year	365	
Interest rate	8	%

Table 5
Key component cost models.

Components	Cost models
Compressors [51]	$Z_C = \frac{71.1}{0.92-\eta_C} m_{CO2} \frac{P_{out}}{P_{in}} \ln\left(\frac{P_{out}}{P_{in}}\right)$
Heat exchanger [52]	$Z_{HE} = 2143A^{0.514}$
HPT [25]	$Z_{HPT} = z_{HPT} V_{HPT}{}^{0.6} + 10000$
Gas holder [27]	$Z_{GH} = z_{GH} V_{GH}$
Turbines [52]	$Z_C = 479.34 \frac{m_{CO2}}{0.93-\eta_T} \ln\left(\frac{P_{in}}{P_{out}}\right)\left(1+e^{0.036T_{in}-54.4}\right)$

$$Z_{elec,p} = z_{elec,p} \cdot n \cdot \int_{t_{s,dis}}^{t_{e,dis}} W_T dt \tag{29}$$

Where $z_{elec,p}$ is the discharging electricity price.

The economic calculation results are shown in Table 6. For the optimized CCES system, the total equipment investment is 29.80 M$. The portion of turbines is the largest, accounting for 56.78 %, and the that of gas holder is smallest, accounting for 1.34 %. The *LCOE* of the system is 0.093 $/kWh, which is lower than reference [33]. Therefore, the system demonstrates commercialization potential, with a net present value (*NPV*) of 58.98 M$ over a 30-year operation period.

4.5. The potential challenges and limitations

The study presents significant advancements in the CCES system design but acknowledges several limitations and challenges that warrant further investigation. Below is a structured discussion of these aspects.

1. Parameter control challenges for HPT: The system relies on precise control of sCO_2 near the pseudo-critical temperature (T_{pc}). Maintaining stable supercritical conditions under dynamic pressure and temperature variations during charging/discharging introduces operational challenges.
2. Economic and scalability concerns: The current economic analysis assumes fixed electricity prices for charging and discharging process, neglecting real-time price fluctuations influenced by demand peaks. Dynamic pricing optimization are required to enhance *NPV*.
3. Deviation between theory and practice: The study neglects pipeline pressure drops, heat losses, and transient effects during start-up and shutdown. The actual round-trip efficiency may be lower than the calculation value.

5. Conclusions

The CCES system serves as a vital solution for meeting contemporary electricity demands and addressing the challenges associated with renewable energy integration. This study presents the construction of a three-stage compression and three-stage expansion CCES system, grounded in the first law of thermodynamics and the principle of mass conservation. Through a dynamic analysis of the CCES system under varying gas storage parameters, we established the relationship between discharge time and storage temperature. The conclusions drawn are as follows.

(1) Innovative storage parameter criteria: Through a comprehensive thermodynamic analysis, we propose new selection criteria for sCO_2 storage parameters, that is elevating $T_{s,dis}$ to the pseudo-critical temperature (T_{pc}). This approach offers a solid basis for optimizing storage conditions and extending the discharging time. Based on the criteria, the discharging time significantly extends from 0.96 h to 3.00 h
(2) Dynamic system development. A novel dynamic CCES system was developed and rigorously analyzed based on thermodynamic modeling. This system serves as a practical model for analysis and enhancing the efficiency of energy storage processes with supercritical fluid.
(3) Enhanced CCES system performance. By optimizing storage parameters according to our proposed criteria, we have achieved a substantial improvement in energy storage density. This advancement not only enhances the overall efficiency of the CCES system but also paves the way for more effective and sustainable energy storage solutions. At storage pressures of 14 MPa, increasing the storage temperature from 35 °C to T_{pc} improves the η_{RT} from 66.50 % to 69.32 %, while raising the energy storage density from 2.71 to 8.74 kWh/m^3.

Table 6
Cost of components and evaluation indicators value.

Components/Parameter	Cost (M$)	Ratio (%)/Unit
Compressors	7.98	26.77
Heat exchangers	2.23	7.48
HPT	2.29	7.68
Gas holder	0.40	1.34
Turbines	16.92	56.78
Total equipment investment	29.80	100
LCOE	0.93	$/kWh
NPV	58.98	M$
Payback Period	5	year

Nomenclature

A	heat transfer area	*x*	dryness fraction
C	compressor	Z	cost
CAES	compressed air energy storage		
CCES	compressed CO_2 energy storage	**Subscripts**	
Cp	specific heat capacity	1, 2, 3 …	state points
CT	cold tank	ave	average
E	output/input energy	char	charging process
ESD	energy storage density	dis	discharging process
h	enthalpy per unit mass, kJ/kg	d	design condition
HE	heat exchanger	e	end
HT	hot tank	elec	electrict
HPT	high-pressure tank	envir	environment
Ir	interest rate	ex	exhaust
k	thermal conductivity	GH	gas holder
LAES	liquid air energy storage	htf	heat transfer fluid
LCES	liquefied CO_2 energy storage	od	off design condition
LCOE	levelized cost of electricity	RTE	round trip efficiency
m	mass flow rate, kg/s	re	relative
N	rotational speed, operational lifetime	tot	total
n	number of cycles	s	start
NPV	Net present value	OM	O&M operations
P	pressure, MPa	p	peak
Q	thermal load, MW	v	Valley
s	entropy		
sCO_2	supercritical carbon dioxide	**Greek symbols**	
T	turbine	α	boiler heat retention coefficient
T	temperature, °C	η	efficiency
t	time	α	boiler heat retention coefficient
u	specific internal energy	β	mass storage density
V	volume, m^3	π	compression ration
W	output/input work, MW	Δ	difference

CRediT authorship contribution statement

Yuandong Guo: Writing – original draft, Validation, Software, Methodology, Investigation, Formal analysis, Data curation, Conceptualization. **Jinliang Xu:** Writing – review & editing, Supervision, Project administration, Investigation, Funding acquisition, Conceptualization.

Xiongjiang Yu: Writing – review & editing, Supervision, Investigation, Funding acquisition, Conceptualization. **Enhui Sun:** Writing – review & editing, Supervision, Investigation. **Jian Xie:** Resources, Investigation, Data curation. **Guanglin Liu:** Software, Resources, Investigation.

Declaration of competing interest

The authors declare that they have no known competing financial interests or personal relationships that could have appeared to influence the work reported in this paper.

Acknowledgements

The authors acknowledge support from the National Natural Science Foundation of China (52130608, 52206197).

Data availability

Data will be made available on request.

References

[1] Yang Y, Tong L, Liu Y, Guo W, Wang L, Qiu Y, et al. A novel integrated system of hydrogen liquefaction process and liquid air energy storage (LAES): energy, exergy, and economic analysis. Energy Convers Manag 2023;280:116799.
[2] Lu Y, Yang X, Bian D, Chen Y, Li Y, Yuan Z, et al. A novel approach for quantifying water resource spatial equilibrium based on the regional evaluation, spatiotemporal heterogeneity and geodetector analysis integrated model. J Clean Prod 2023;424:138791.
[3] Abouzeid SI, Guo Y, Zhang H-C. Cooperative control framework of the wind turbine generators and the compressed air energy storage system for efficient frequency regulation support. Int J Electr Power Energy Syst 2021;130:106844.
[4] Ding X, Duan L, Li D, Ji S, Yang L, Zheng N, et al. Dynamic characteristics of a novel liquid air energy storage system coupled with solar heat and waste heat recovery. Renew Energy 2024;221:119780.
[5] Jiang B, Hu X, Söderlind U, Göransson K, Zhang W, Yu C. Identification of the biomethanation pathways during biological CO2 fixation with exogenous H2 addition. Fuel Process Technol 2022;238:107478.
[6] Vilanova MRN, Flores AT, JapjjotBSoMS Balestieri. Engineering. Pumped hydro storage plants. a review 2020;42.
[7] Li Y, Wei Y, Zhu F, Du J, Zhao Z, Ouyang M. The path enabling storage of renewable energy toward carbon neutralization in China. eTransportation 2023; 16:100226.
[8] Rehman S, Al-Hadhrami LM, Alam MM. Pumped hydro energy storage system: a technological review. Renew Sustain Energy Rev 2015;44:586–98.
[9] Zhou Y, Zhang H, Ji S, Sun M, Ding X, Zheng N, et al. Whole process dynamic performance analysis of a solar-aided liquid air energy storage system: from single cycle to multi-cycle. Appl Energy 2024;373:123938.
[10] King M, Jain A, Bhakar R, Mathur J, Wang J. Overview of current compressed air energy storage projects and analysis of the potential underground storage capacity in India and the UK. Renew Sustain Energy Rev 2021;139:110705.
[11] Manzoni M, Patti A, Maccarini S, Traverso A. Analysis and comparison of innovative large scale thermo-mechanical closed cycle energy storages. Energy 2022;249:123629.
[12] Sciacovelli A, Li Y, Chen H, Wu Y, Wang J, Garvey S, et al. Dynamic simulation of Adiabatic compressed air energy storage (A-CAES) plant with integrated thermal storage – link between components performance and plant performance. Appl Energy 2017;185:16–28.
[13] Xu W, Zhao P, Liu A, Wu W, Wang J. Design and off-design performance analysis of a liquid carbon dioxide energy storage system integrated with low-grade heat source. Appl Therm Eng 2023;228:120570.
[14] Guizzi GL, Manno M, Tolomei LM, Vitali RM. Thermodynamic analysis of a liquid air energy storage system. Energy 2015;93:1639–47.
[15] Kantharaj B, Garvey S, Pimm A. Thermodynamic analysis of a hybrid energy storage system based on compressed air and liquid air. Sustain Energy Technol Assessments 2015;11:159–64.
[16] Alami AH, Hawili AA, Hassan R, Al-Hemyari M, Aokal K. Experimental study of carbon dioxide as working fluid in a closed-loop compressed gas energy storage system. Renew Energy 2019;134:603–11.
[17] Zhu R, Han B-c, Dong K, Wei G-s. A review of carbon dioxide disposal technology in the converter steelmaking process. Int J Miner Metall Mater 2020;27:1421–9.
[18] Liu Z, Guan H, Shao J, Jin X, Su W, Zhang H, et al. Thermodynamic and advanced exergy analysis of a trans-critical CO2 energy storage system integrated with heat supply and solar energy. Energy 2024;302:131507.
[19] Liu Z, Guan H, Jin X, Su W, Shao J, Fan J, et al. Thermodynamic and economic analysis of a trans-critical CO2 energy storage system integrated with ORC and solar energy. Energy 2024;313:133667.
[20] Huang Q, Wang W, Ma C, Feng B, Luan J, Sun Q, et al. Assessment of the arbitrage by a compressed CO2 energy storage system-based on dynamic characteristics. J Energy Storage 2024;95:112391.
[21] Deng C, Zhang L, Gan M, Wang Y, Li X. Economic and environmental feasibility of coupled wind power-subsurface compressed CO2 energy storage system in China: an LCA approach. Gas Sci Eng 2024;128:205399.
[22] Liu S, Wu S, Hu Y, Li H. Comparative analysis of air and CO2 as working fluids for compressed and liquefied gas energy storage technologies. Energy Convers Manag 2019;181:608–20.
[23] Stanek B, Ochmann J, Bartela Ł, Brzuszkiewicz M, Rulik S, Waniczek S. Isobaric tanks system for carbon dioxide energy storage – the performance analysis. J Energy Storage 2022;52:104826.
[24] Liu H, He Q, Borgia A, Pan L, Oldenburg CM. Thermodynamic analysis of a compressed carbon dioxide energy storage system using two saline aquifers at different depths as storage reservoirs. Energy Convers Manag 2016;127:149–59.
[25] Xu M, Wang X, Wang Z, Zhao P, Dai Y. Preliminary design and performance assessment of compressed supercritical carbon dioxide energy storage system. Appl Therm Eng 2021;183:116153.
[26] Astolfi M, Rizzi D, Macchi E, Spadacini C. A novel energy storage system based on carbon dioxide unique thermodynamic properties. J Eng Gas Turbines Power 2022; 144(8).
[27] Liu Z, Yan X, Wang S, Wei X, Zhang Y, Ding J, et al. Performance of compressed CO2 energy storage systems with different liquefaction and storage scenarios. Fuel 2024;359:130527.
[28] Wang M, Zhao P, Yang Y, Dai Y. Performance analysis of energy storage system based on liquid carbon dioxide with different configurations. Energy 2015;93: 1931–42.
[29] Sun W, Liu X, Yang X, Yang X, Liu Z. Design and thermodynamic performance analysis of a new liquid carbon dioxide energy storage system with low pressure stores. Energy Convers Manag 2021;239:114227.
[30] Liu X, Yan X, Liu X, Liu Z, Zhang W. Comprehensive evaluation of a novel liquid carbon dioxide energy storage system with cold recuperator: energy, conventional exergy and advanced exergy analysis. Energy Convers Manag 2021;250:114909.
[31] He T, Cao Y, Si F. Thermodynamic analysis and optimization of a compressed carbon dioxide energy storage system coupled with a combined heating and power unit. Energy Convers Manag 2023;277:116618.
[32] Sun L, Tang B, Xie Y. Performance assessment of two compressed and liquid carbon dioxide energy storage systems: thermodynamic, exergoeconomic analysis and multi-objective optimization. Energy 2022;256:124648.
[33] Zhao P, Xu W, Zhang S, Gou F, Wang J, Dai Y. Components design and performance analysis of a novel compressed carbon dioxide energy storage system: a pathway towards realizability. Energy Convers Manag 2021;229:113679.
[34] Wang Q, Ma X, Xu J, Li M, Wang Y. The three-regime-model for pseudo-boiling in supercritical pressure. Int J Heat Mass Tran 2021;181:121875.
[35] Dong M, Xu J, Wang Y. Critical threshold for bubble-like nucleation during pseudoboiling at supercritical pressures. Langmuir 2024;40(25):13276–91.
[36] Cao Z, Deng J, Zhou S, He Y. Research on the feasibility of compressed carbon dioxide energy storage system with underground sequestration in antiquated mine goaf. Energy Convers Manag 2020;211:112788.
[37] Zhang Y, Wu Y, Yang K. Dynamic characteristics of a two-stage compression and two-stage expansion compressed carbon dioxide energy storage system under sliding pressure operation. Energy Convers Manag 2022;254:115218.
[38] He Q, Liu H, Hao Y, Liu Y, Liu W. Thermodynamic analysis of a novel supercritical compressed carbon dioxide energy storage system through advanced exergy analysis. Renew Energy 2018;127:835–49.
[39] Zhang N, Cai R. Analytical solutions and typical characteristics of part-load performances of single shaft gas turbine and its cogeneration. Energy Convers Manag 2002;43(9):1323–37.
[40] Wang W, Cai R, Zhang N. General characteristics of single shaft microturbine set at variable speed operation and its optimization. Appl Therm Eng 2004;24(13): 1851–63.
[41] Ma T, Li M-J, Xu J-L, Ni J-W, Tao W-Q, Wang L. Study of dynamic response characteristics of S-CO2 cycle in coal-fired power plants based on real-time micro-grid load and a novel synergistic control method with variable working conditions. Energy Convers Manag 2022;254:115264.
[42] Kim HJ, Ahn JM, Cho SO, Cho KR. Numerical simulation on scroll expander–compressor unit for CO2 trans-critical cycles. Appl Therm Eng 2008;28 (13):1654–61.
[43] Guo C, Xu Y, Guo H, Zhang X, Lin X, Wang L, et al. Comprehensive exergy analysis of the dynamic process of compressed air energy storage system with low-temperature thermal energy storage. Appl Therm Eng 2019;147:684–93.
[44] Zhang Y, Yang K, Li X, Xu J. Thermodynamic analysis of energy conversion and transfer in hybrid system consisting of wind turbine and advanced adiabatic compressed air energy storage. Energy 2014;77:460–77.
[45] Deng Y, Wang J, Cao Y, Zhang X, Zhang N, He G, et al. Technical and economic evaluation of a novel liquid CO2 energy storage-based combined cooling, heating, and power system characterized by direct refrigeration with phase change. Appl Therm Eng 2023;230:120833.
[46] Huang Q, Feng B, Liu S, Ma C, Li H, Sun Q. Dynamic operating characteristics of a compressed CO2 energy storage system. Appl Energy 2023;341:120985.
[47] Fu H, He Q, Song J, Hao Y. Thermodynamic of a novel solar heat storage compressed carbon dioxide energy storage system. Energy Convers Manag 2021; 247:114757.
[48] Zhao T, He Y, Deng J. Effect of geothermal heat transfer on performance of the adiabatic compressed air energy storage systems with the salt cavern gas storage. Appl Therm Eng 2024;249:123386.

[49] Zhao R, Liu Z. Thermo-economic performance of a compressed CO2 energy storage system with a flexible gas holder. J Energy Storage 2023;60:106675.

[50] Aghagoli A, Sorin M. CFD modelling and exergy analysis of a heat pump cycle with tesla turbine using CO2 as a working fluid. Appl Therm Eng 2020;178:115587.

[51] Akbari AD, Mahmoudi SMS. Thermoeconomic analysis & optimization of the combined supercritical CO2 (carbon dioxide) recompression brayton/organic rankine cycle. Energy 2014;78:501–12.

[52] Wang X, Dai Y. An exergoeconomic assessment of waste heat recovery from a gas turbine-modular helium reactor using two transcritical CO2 cycles. Energy Convers Manag 2016;126:561–72.